

Recrystallisation and damage of ice in winter sports

Alexandra Seymour-Pierce, Ben Lishman, Peter Sammonds

Keywords: Ice, friction, winter sport, skeleton, recrystallization, fracture

Abstract

Ice samples, after sliding against a steel runner, show evidence of recrystallization and microcracking under the runner, as well as macroscopic cracking throughout the ice. The experiments which produced these ice samples are designed to be analogous to sliding in the winter sport of skeleton. Changes in the ice fabric are shown using thick and thin sections under both diffuse and polarised light. Ice drag is estimated as 40-50% of total energy dissipation in a skeleton run. The experimental results are compared to visual inspections of skeleton tracks, and to similar behaviour in rocks during sliding on earthquake faults. The results presented may be useful to athletes and designers of winter sports equipment.

Introduction

In several winter sports – skeleton and speed skating, for example – athletes aim to slide as fast as possible over ice without losing control. Typically a long and narrow metal contact (slider) supports the athlete's weight on the ice. This contact indents the ice, and this indentation leads to preferential sliding in the direction of the long face of the slider. Skates and sled runners consequently slide much more easily along their length than across it. The athlete is slowed down by air resistance, frictional resistance, indentation processes, and, occasionally, deliberate braking (for example when skeleton athletes put a foot down). Steering is achieved by manipulating the same forces (for example by the athlete using her weight to deform a skeleton sled slightly, creating asymmetric friction and a steering moment). Understanding these forces, and their role in slowing, steering and controlling winter sports participants, is complicated. One route to an understanding of ice friction and indentation is to look at the marks that sliding leaves on the ice.

In this paper we focus on the sport of skeleton, which was introduced as a Winter Olympic sport in 2002. Athletes begin at the top of an ice track (typically 1-2km long) with a sprint start, from which they dive onto their sled, and lie head first with their legs extended behind them to slide down the track (figure 1). Speeds can reach over 35m/s, and in corners athletes can experience forces of several g .

The interaction between the ice and the runner is controlled by a combination of friction and ploughing, i.e. macroscopic ice deformation by the runner (Lozowski et al., 2014). The friction of ice is complicated, since ice often exists at temperatures very close to its melting point. Phenomenological models of ice friction typically incorporate asperity-asperity resistance, melting and lubrication, and softening of the ice (Bowden and Tabor, 1939; Oksanen and Keinonen, 1982; Hatton et al., 2009; Persson, 2015). Ice friction also has memory: the instantaneous friction depends on the sliding history, as well as the instantaneous sliding conditions (Lishman et al., 2011). Measuring friction in the skeleton *in situ* would require measurement of the shear force between ice and runner, which is difficult to achieve. However, the energy dissipated by this shear force may leave traces on the ice, which allow us to make inferences about the drag on the sled. In the next section of this paper we estimate this energy dissipation.

Energy balance in the skeleton

In this section we estimate the energy transmitted into the ice over the course of a single skeleton run (cf. Bromley, 1999; Roche et al., 2008; Baumann, 1973).

Energy is added to the system of sled and athlete by the running start, and by the effects of gravity. At the finish line, the system has some kinetic energy, and some energy has been dissipated.

$$E_{start} + E_{gravitational} = E_{kinetic} + E_{dissipated} \quad (1)$$

We assume that all energy from the push start is converted to kinetic energy. This is convenient, since the speed at the end of the push start is measured at many skeleton events. Energy dissipated during the push start is therefore not included in our model.

Rearranging,

$$E_{dissipated} = mgh - \frac{1}{2}m(v_{finish}^2 - v_{start}^2) \quad (2)$$

where v_{finish} and v_{start} represent the speeds at the end of the start phase, and at the finish line, respectively, and h is the vertical drop of the track. The two mechanisms of energy dissipation are air drag and ice drag. In this case ice drag can include both the ongoing frictional drag under the runners, and discrete events: for example, if the sled hits a wall or the athlete puts a foot on the ice. To calculate the air drag, we assume constant acceleration, and integrate the Rayleigh drag equation to give

$$E_{air\ drag} = \frac{1}{2}\rho c_d A_f (v_{start}^2 l + al^2) \quad (3)$$

where ρ is the density of the air, c_d is a drag coefficient, A_f is the area perpendicular to motion (i.e. the cross sectional area of the athlete's head and shoulders and the sled) and l is the length of the track.

We can then calculate the energy transmitted into the ice over the course of a single run:

$$E_{ice\ drag} = mgh - \frac{1}{2}m(v_{finish}^2 - v_{start}^2) - \frac{1}{2}\rho c_d A_f (v_{start}^2 l + al^2) \quad (4)$$

Equation 4 allows us to calculate the energy transmitted into the ice in a given run. Track specifications (for the 15 recognised tracks) and race times and speeds (for official races going back to 2006) are given at www.ibsf.org (the website of the International Bobsleigh and Skeleton Foundation). We use the women's gold medal winning run (run 4) from the 2014-15 World Championship, held at Winterberg, Germany, as a test case. The Winterberg track has length $l=1330m$ and drop $h=110m$; $v_{start}=17.08ms^{-1}$ and $v_{finish}=36.14ms^{-1}$. We assume an athlete mass of 70kg and a sled mass of 35kg, so $m=105kg$. We assume $c_d=0.45$ (an equivalent drag coefficient to a hemisphere) and $A_f=0.135m^2$ (based on approximate projections of a helmet, shoulders, and the sled.)

Using these numbers we find that the gravitational energy is 113.3kJ, the initial kinetic energy is 15.3kJ, and the final kinetic energy is 68.6kJ. The energy dissipated is therefore 60kJ. Of this, 35.5kJ

is lost to air drag, and 24.5kJ is lost to ice drag. Put differently, of the available input energy, around half is dissipated, and of this dissipated energy, around 60% is lost to air drag and 40% to ice drag. These results remain reasonably consistent when different tracks and runs are used, although heavier athletes (e.g. most men) tend to lose more energy to ice drag (up to 60% - this occurs since air drag is independent of weight but the initial potential energy increases with weight). These results rest on the assumptions that air drag is well represented by a Rayleigh model, that acceleration is constant throughout the run, and that the air drag coefficient is comparable to that of a hemisphere. The results also represent an average over the whole run and do not provide information on instantaneous changes in the balance between air drag and ice drag; for example, we might expect ice drag to dominate in the corners of a track, where centripetal forces lead to higher normal forces, and air drag to dominate in the straight sections of a track.

The ice drag of 24.5kJ given above represents both the heat generated by frictional sliding and the energy lost during any impacts with the ice. The heat generated by frictional sliding may cause melting and softening of the ice at the ice-runner interface, while the energy dissipated during impacts may cause fracturing at the ice surface or within the ice. Both of these processes leave traces on or in the ice; these traces are the focus of this paper and are discussed in later sections. The frictional component of the ice drag is generated at the ice-runner interface (a thin lubricating water layer may also be present). The energy, released as heat, will warm the runner and the ice. Runners are fabricated from carbon steel bars. Each runner weighs around 1.6kg, and so if all the 24.5kJ of energy were conducted into the runners, their temperature would rise by around 15K (neglecting heat lost to the air). This doesn't happen: the runners are cold and frequently ice-covered at the end of races. Further, since the ice is constantly replenished, the interface temperature remains very close to 0°C, and so any warming of the runners will lead to a thermal imbalance at the interface and increased heat conduction into the ice. Further analysis is needed to determine the precise fraction of heat conducted into the ice.

The energy of ice drag also allows calculation of an effective friction coefficient. Assuming Amontons'-type behaviour, $F=\mu N$, and

$$\mu_{effective} = \frac{E_{ice\ drag}}{l N} \quad (5)$$

This gives a coefficient of $\mu_{effective} = 0.018$, which provides an upper bound on the average sliding friction coefficient during a run on the skeleton track (since some components of the energy of ice drag will come from discrete events). This value gives a good match to predictions from the literature (Oksanen and Keinonen, 1982; Lozowski and Szilder, 2011; Akkok et al., 1987; Evans et al., 1976; Stiffler, 1984).

In the rest of this paper we investigate how the ice drag components of energy dissipation and frictional heat generation affect the ice structure.

Experimental methods

A series of experiments were conducted in the cold laboratory of University College London between 2012 and 2014. The tribometer shown in figure 2 was used to measure the behaviour of a steel

runner sliding on ice. The tribometer is a 1.2m pin-on-disc design, after Bäurle et al., (2006), consisting of a stationary slider positioned on a revolving ice surface.

The ice track is prepared from tap water, boiled to remove dissolved gases and minimise ice porosity. This water is filtered to remove particulates and left to freeze in a container at -3°C , covered with a cloth to exclude outside particles (the relatively high temperature allows the diffusion of air bubbles (Bari and Hallett, 1974)). This ice was then broken up and passed through a commercial ice-crushing machine, before being passed through a 3.35mm sieve. Two different sets of tracks were made: one from the small grains ($<3.35\text{mm}$ diameter) and one from the large grains ($>3.35\text{mm}$ diameter). These ice seeds were then packed into the annulus and flooded with deaerated water close to its freezing point. The resulting slurry was checked for air pockets, and those found were manually pierced to allow complete saturation. The ice-water slurry was allowed to freeze completely, and then left to sublime for 24 hours to give a flatter and more consistent ice surface. The use of a slurry, rather than pure water, leads to lower expansion and thus reduces residual stresses in the ice. The ice thickness used was 4cm, which is comparable to track ice thicknesses.

The slider used for these experiments was an 85mm-long square steel bar (16mm side), curved upwards at either end. The normal load is 200N, and so the pressure under the slider is 294kPa (for comparison, typical track pressures might be 5MPa). Experiments were conducted at 6m/s, and run for 1km (i.e. around 160s). This means that our slider covers the same ice track many times, and so the results presented here are likely to be more pronounced than those on the skeleton track. Countering this, the pressure and slider length in these experiments are significantly lower than those on the track. It's worth noting one important source of error: the experiments use a straight slider on a round track, and so some radial forces will have been generated alongside the desired circumferential forces. The straight slider was used to allow experiments to be more easily conducted (since a curved slider would only be matched to one specific sliding radius). We believe that the radial forces will have little effect on well-lubricated, Amontons'-type sliding friction, since the resistive forces will be overwhelmingly along the length of the slider. However, when fracture and indentation occur, effects at the front of the slider (for example ploughing of the ice) will be misaligned with the middle of the slider, and so these effects may be amplified. However, we believe that all the qualitative results shown here would still be observed with a linear tribometer, and we also note that the actual sport of skeleton frequently features normal sliding as well as down-track sliding.

Experiments were conducted at -7°C , -3°C , and -0.5°C . After each experiment, ice blocks were cut away from the track for analysis (see figure 3). Thick and thin sections of the deformed ice and undeformed ice were analysed under diffuse light and crossed polars. Thick and thin sections of the undeformed track with small grains ($<3.35\text{mm}$), frozen at -7°C , -3°C , and -0.5°C , are shown in figures 4-6. For comparison, we also show the structure of larger-grained ice manufactured at -0.5°C (figure 7).

Results

The deformation of the ice track which occurs during sliding can be seen in figures 8-11 (which are the after-sliding equivalent of figures 4-7, respectively). At all temperatures, extensive inelastic deformation is seen, consisting of a concentrated damage zone extending the width of the slider. At colder ice temperatures, the damage zone extends down into the ice track in the form of cracks,

which radiate from the initial damage zone (figures 9 and 10). For both coarse- and fine-grained ice, recrystallisation is seen under the slider at $T_i = -0.5^\circ\text{C}$ (figures 7 and 11); this change in microstructure is visible under crossed polars and the regions of recrystallisation are highlighted. By “recrystallisation”, we mean here a process under which the grains rearrange into a new structure (frequently with an associated change in typical grain size) under the influence of heat, and possibly pressure: in this work, these changes in grain structure are visible on thin section photographs.

Discussion

These results show that two different processes occur in the ice during high speed sliding. The recrystallisation at $T_i = -0.5^\circ\text{C}$ is clear evidence of melt generation under the slider, strongly suggesting that lubrication is the reason for the low coefficient of friction seen at this temperature. However, at colder temperatures, fracture and inelastic deformation clearly dominate any recrystallisation that may occur. Both these processes – the melting or softening which causes recrystallisation, and the initiation and propagation of cracking – represent a transfer of energy into the ice from the sled runners. Observations from our tribometer experiments suggest that as well as the temperature control on cracking and melting, both behaviours are more prevalent with increasing sliding speed.

We believe that the cracks seen in figures 8-11 represent two different behaviours. First, a damaged zone of microcracking is seen directly underneath the runner. Secondly, macroscopic cracks propagate through the ice. Macroscopic cracking is more prominent in larger-grained samples: this indicates that the behaviour of ice during high speed sliding shows a decrease in terminal failure stress of ice with increasing grain size. Other observed brittle failure includes cracking along the length of the track surface as a precursor to spalling (see figure 12), which is perhaps comparable to “crushing with flaking” observed in pure indentation experiments (Tuhkuri, 1995). It seems like that the indenter forces are not spread uniformly across the ice at any instant, but are supported by a few high-pressure zones (Sodhi, 2001). However, the cumulative recrystallisation and microcracking observed are continuous under the slider.

Similar deformation mechanisms to those shown in figure 12 are seen on the skeleton track (figure 13). The main evidence of cracking on the skeleton track is a milky-white appearance of the ice in the corners of the tracks where the centripetal accelerations cause athletes to follow similar lines every run (see figure 13c). Overall, we believe these results suggest that fracture is an important component of the ice drag on the skeleton.

Qualitative comparisons of deformation mechanisms can also be made to rock mechanics. The recrystallisation mechanism seen in the ice at $T_i = -0.5^\circ\text{C}$ appears very similar to that observed during high speed rotary shear experiments with rock, as shown in figure 14. Recrystallisation occurs when the high speed slip of the rock generates enough heat to melt the surfaces. The lubrication then reduces the coefficient of friction, resulting in sudden slip of the rock faces (Smith et al., 2013). It is this behaviour which leads to earthquakes (Goldsby and Tullis, 2011; Golding et al., 2010; Di Toro et al., 2011).

These results suggest avenues for further research. Cutting out sections of skeleton tracks seems unfeasible. However, it should be possible to investigate melting and softening of ice on the track by measuring track surface temperatures. Thermal imaging cameras, either sled-mounted or fixed, could reveal regions of melted ice, and therefore indicate where on the track recrystallisation is likely to be prevalent. Similarly, acoustic sensors deployed on the track or sled could measure cracking, both large and small. One possible application of acoustic sensors would be to provide

immediate feedback to the athlete via an earpiece: athletes could then try to control their sliding to minimise ice fracture. Overall, an improvement in our understanding of ice deformation under the sled will enable improved runner design and sled design.

Conclusions

Estimates suggest that around 40% of the energy dissipated in the skeleton during sliding (or around 20% of the total energy input) is transmitted into the ice. We have conducted laboratory experiments which are analogous to winter sliding sports such as the skeleton. These experiments show three clear ways in which this dissipated energy affects the ice: (a) at high temperatures, sliding causes melting and softening of a surface layer, leading to recrystallisation; (b) at all temperatures, sliding causes microscopic fracturing leading to a damaged zone immediately under the runner (we believe that this damaged zone is equivalent to the milky-white runner-marks seen on the corners of skeleton tracks); and (c) at low temperatures macroscopic fracturing occurs, particularly in large-grained ice. We show that our laboratory results are similar to track observations, and also to observations of recrystallisation in rock mechanics. These results may be useful to designers of winter sports equipment.

Acknowledgments

The authors thank UK Sport for funding and track access. We also thank John Bowles, Neil Hughes, and Steve Boon for supporting the experiments.

Figure Captions

Figure 1: the different phases of the skeleton run. The athlete begins by sprinting while pushing the sled (**a**); dives onto the moving sled (**b**); and slides down the course, head first, on the sled (**c**).

Figure 2: Experimental apparatus. The tribometer has a slider on a fixed arm, which rests on a rotating annulus of ice. The outer diameter of the ice annulus is 1.2m.

Figure 3: Preparing the track for fabric analysis. A section of the track is cut out (**a**), removed from the tribometer (**b**), and cut to size on the bandsaw (**c**). Image (**d**) shows the geometry of the cuts.

Figure 4: Thick (**a**, 5mm) and thin (**b**, 1mm) sections of undeformed ice, $T_i = -0.5^\circ\text{C}$. The section shown is 100mm wide.

Figure 5: Thick (**a**, 5mm) and thin (**b**, 1mm, and **c**, 0.5mm) sections of undeformed ice, $T_i = -3^\circ\text{C}$. The section shown is 120mm wide.

Figure 6: Thick (**a**, 5mm) and thin (**b**, 1mm, and **c**, 0.5mm) sections of undeformed ice, $T_i = -7^\circ\text{C}$. The large crack on the right hand side of the images occurred during sample preparation on the bandsaw. The section shown is 105mm wide.

Figure 7: Thick (**a**, 5mm) and thin (**b**, 1mm) sections of undeformed ice, $T_i = -0.5^\circ\text{C}$, ice seeds $>3.35\text{mm}$. The section shown is 125mm wide.

Figure 8: Thick (**a**, 5mm) and thin (**b**, 1mm, and **c**, 0.5mm) sections of deformed ice, $T_i = -0.5^\circ\text{C}$. The extent of deformation is visible in (**a**) and cracking, which occurred around meltwater during manufacturing, is highlighted in (**b**). Recrystallisation under the slider is highlighted in the white box.

Figure 9: Thick (**a**, 5mm, sample 1, and **b**, 5mm, sample 2) and thin (**c**, 1mm, sample 2) sections of deformed ice, $T_i = -3^\circ\text{C}$, for two different samples (sample 1 is small-grained; sample 2 is large-grained). A damaged zone under the slider is visible in both samples, and fracture networks have propagated through sample 2. No recrystallisation was observed.

Figure 10: Thick (**a**, 5mm, sample 1, and **b**, 5mm, sample 2) and thin (**c**, 1mm, sample 2) sections of deformed ice, $T_i = -7^\circ\text{C}$, for two different samples (sample 1 is small-grained, and sample 2 is large-grained). A damaged zone under the slider is visible in both samples, and fracture networks have propagated through sample 2. No recrystallisation was observed.

Figure 11: Thick (**a**, 5mm) and thin (**b**, 1mm, and **c**, 0.5mm) sections of deformed ice, $T_i = -0.5^\circ\text{C}$, for seed grain size $>3.35\text{mm}$. Recrystallisation under the slider is highlighted.

Figure 12: Illustration of the different types of cracks visible on the ice surface after high speed sliding: (a) $T_i = -0.5^\circ\text{C}$, $v = 6\text{ms}^{-1}$; (b) $T_i = -3^\circ\text{C}$, $v = 10\text{ms}^{-1}$; (c) $T_i = -10^\circ\text{C}$, $v = 10\text{ms}^{-1}$.

Figure 13: Illustration of the inelastic deformation mechanisms observed on the skeleton track: (a) brittle failure, evidenced by sharp-edged cavities in the ice; (b) large cracks, several centimetres long; (c) micro-cracking, evidenced by a milky-white zone, occurring frequently in high- g corners.

Figure 14: Comparison of recrystallisation mechanisms in ice (a, this study) and rock (b). The ice thin sections are from this study, recrystallisation in rock from Smith et al. (2013).

References

- Akkok, M., Ettles, C. M., & Calabrese, S. J. (1987). Parameters affecting the kinetic friction of ice. *Journal of tribology*, 109(3), 552-559.
- Bari, S. A., & Hallett, J. (1974). Nucleation and growth of bubbles at an ice-water interface. *Journal of Glaciology*, 13, 489-520.
- Baumann, W. (1973). The influence of mechanical factors on speed in tobogganing. In Cerquigline, S., Venerando, A., and Wartenwiler, J., editors, *Biomechanics III*, volume 8, pages 453-459. Karger, Basel.
- Bäurle, L., Szabo, D., Fauve, M., Rhyner, H., & Spencer, N. D. (2006). Sliding friction of polyethylene on ice: tribometer measurements. *Tribology Letters*, 24(1), 77-84.
- Bowden, F. P., & Hughes, T. P. (1939). The mechanism of sliding on ice and snow. In *Proceedings of the Royal Society of London A: Mathematical, Physical and Engineering Sciences* (Vol. 172, No. 949, pp. 280-298). The Royal Society.
- Bromley, K. (1999). Factors affecting the performance of skeleton bobsleds. PhD thesis, University of Nottingham.
- Di Toro, G., Han, R., Hirose, T., De Paola, N., Nielsen, S., Mizoguchi, K., ... & Shimamoto, T. (2011). Fault lubrication during earthquakes. *Nature*, 471 (7339), 494-498.
- Evans, D. C. B., Nye, J. F., & Cheeseman, K. J. (1976, January). The kinetic friction of ice. In *Proceedings of the Royal Society of London A: Mathematical, Physical and Engineering Sciences* (Vol. 347, No. 1651, pp. 493-512). The Royal Society.
- Golding, N., Schulson, E. M., & Renshaw, C. E. (2010). Shear faulting and localized heating in ice: The influence of confinement. *Acta materialia*, 58 (15), 5043-5056.
- Goldsby, D. L., & Tullis, T. E. (2011). Flash heating leads to low frictional strength of crustal rocks at earthquake slip rates. *Science*, 334(6053), 216-218.
- Hatton, D. C., Sammonds, P. R., & Feltham, D. L. (2009). Ice internal friction: Standard theoretical perspectives on friction codified, adapted for the unusual rheology of ice, and unified. *Philosophical Magazine*, 89(31), 2771-2799.
- Lishman, B., Sammonds, P., & Feltham, D. (2011). A rate and state friction law for saline ice. *Journal of Geophysical Research: Oceans* (1978–2012), 116 (C5).
- Lozowski, E. P., & Szilder, K. (2011). FAST 2.0 derivation and new analysis of a hydrodynamic model of speed skate ice friction. In *The Twenty-first International Offshore and Polar Engineering Conference*. International Society of Offshore and Polar Engineers.
- Lozowski, E., Szilder, K., Maw, S., & Morris, A. (2014). A Model of Ice Friction for Skeleton Sled Runners. In *The Twenty-fourth International Ocean and Polar Engineering Conference*. International Society of Offshore and Polar Engineers.
- Oksanen, P., & Keinonen, J. (1982). The mechanism of friction of ice. *Wear*, 78(3), 315-324.
- Persson, B. N. J. (2015). Ice friction: Role of non-uniform frictional heating and ice premelting. *The Journal of chemical physics*, 143(22), 224701.
- Roche, J., Turnock, S., & Wright, S. (2008). An Analysis of the Interaction Between Slider Physique and Descent Time for the Bob Skeleton (P153). In *The Engineering of Sport 7* (pp. 101-109). Springer Paris.
- Sodhi, D. S. (2001). Crushing failure during ice–structure interaction. *Engineering Fracture Mechanics*, 68(17), 1889-1921.

- Stiffler, A. K. (1984). Friction and wear with a fully melting surface. *Journal of tribology*, 106(3), 416-419.
- Tuhkuri, J. (1995). Experimental observations of the brittle failure process of ice and ice-structure contact. *Cold regions science and technology*, 23(3), 265-278.



(a) sprint phase



(b) loading phase



(c) sliding phase

Figure 1: the different phases of the skeleton run. The athlete begins by sprinting while pushing the sled (**a**); dives onto the moving sled (**b**); and slides down the course, head first, on the sled (**c**).

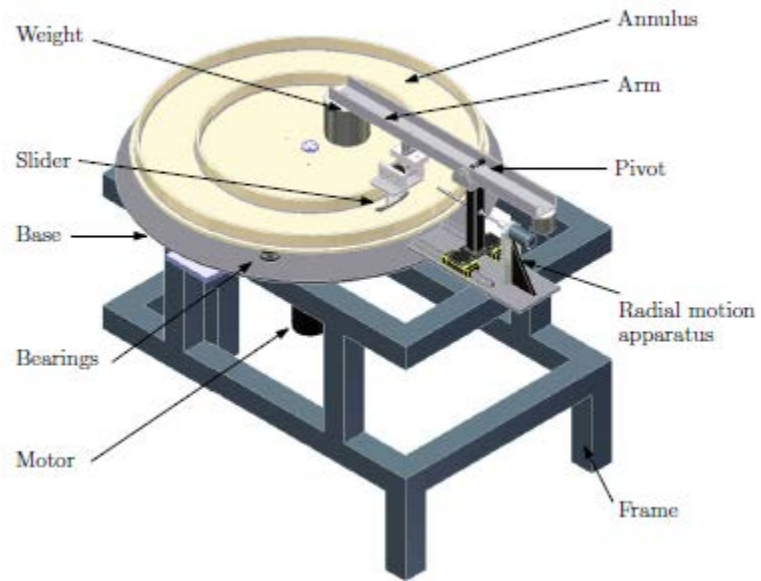


Figure 2: Experimental apparatus. The tribometer has a slider on a fixed arm, which rests on a rotating annulus of ice. The outer diameter of the ice annulus is 1.2m.

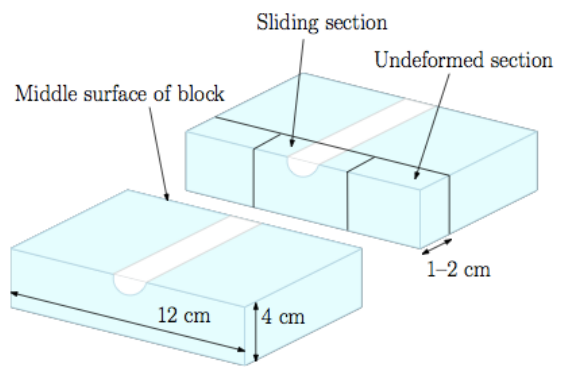


Figure 3: Preparing the track for fabric analysis. A section of the track is cut out (a), removed from the tribometer (b), and cut to size on the bandsaw (c). Image (d) shows the geometry of the cuts.

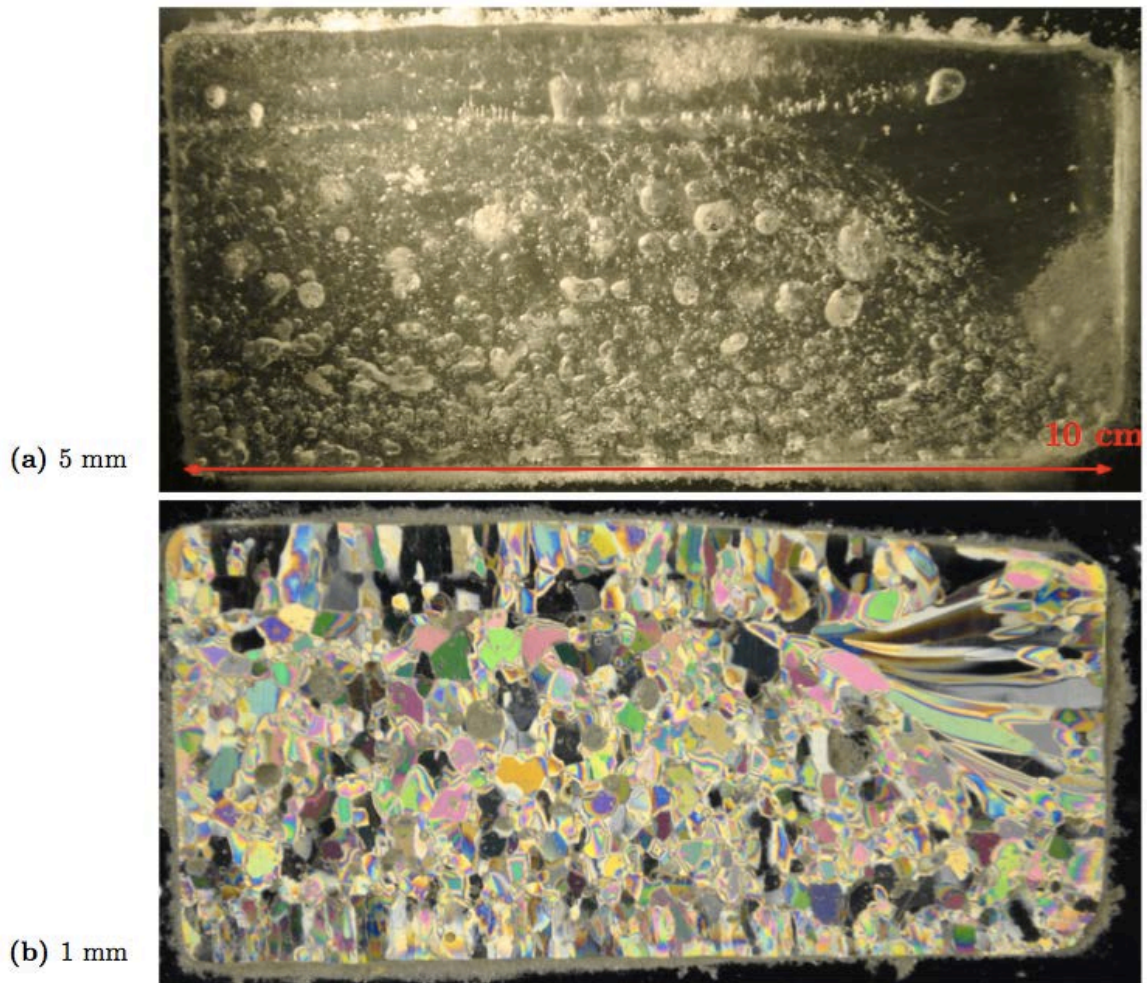
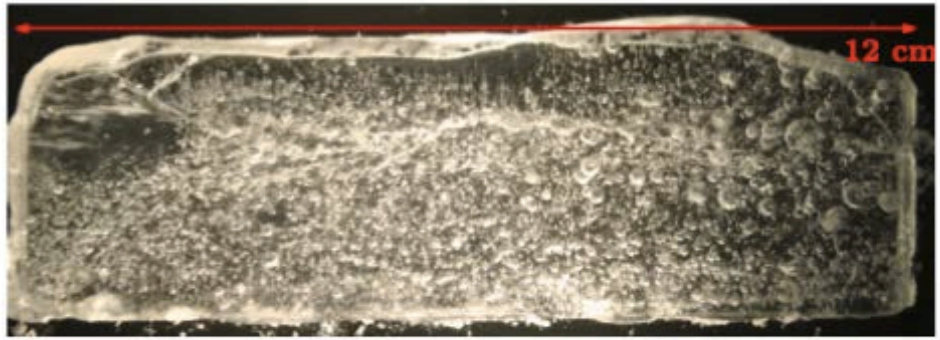
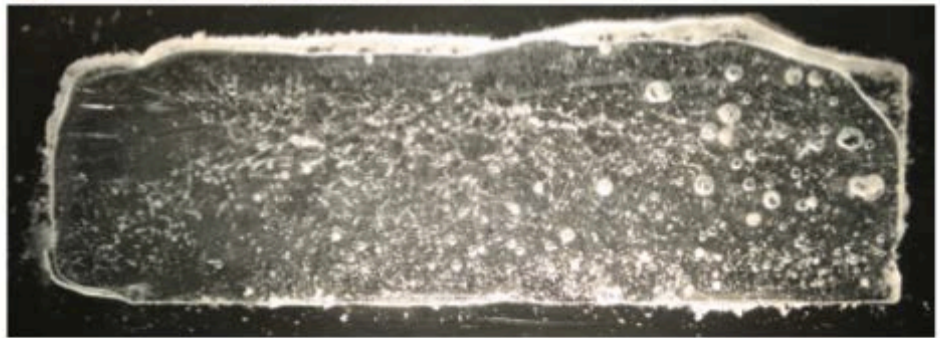


Figure 4: Thick (a, 5mm) and thin (b, 1mm) sections of undeformed ice, $T_i = -0.5^\circ\text{C}$. The section shown is 100mm wide.

(a) 5 mm



(b) 1 mm



(c) 0.5 mm

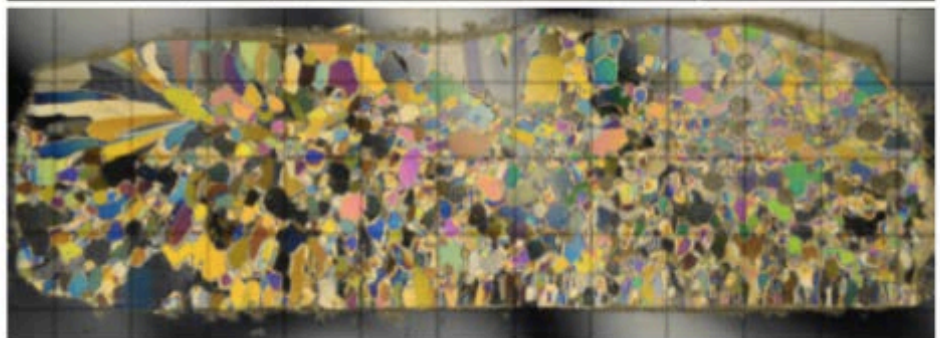


Figure 5: Thick (a, 5mm) and thin (b, 1mm, and c, 0.5mm) sections of undeformed ice, $T_i = -3^\circ\text{C}$. The section shown is 120mm wide.

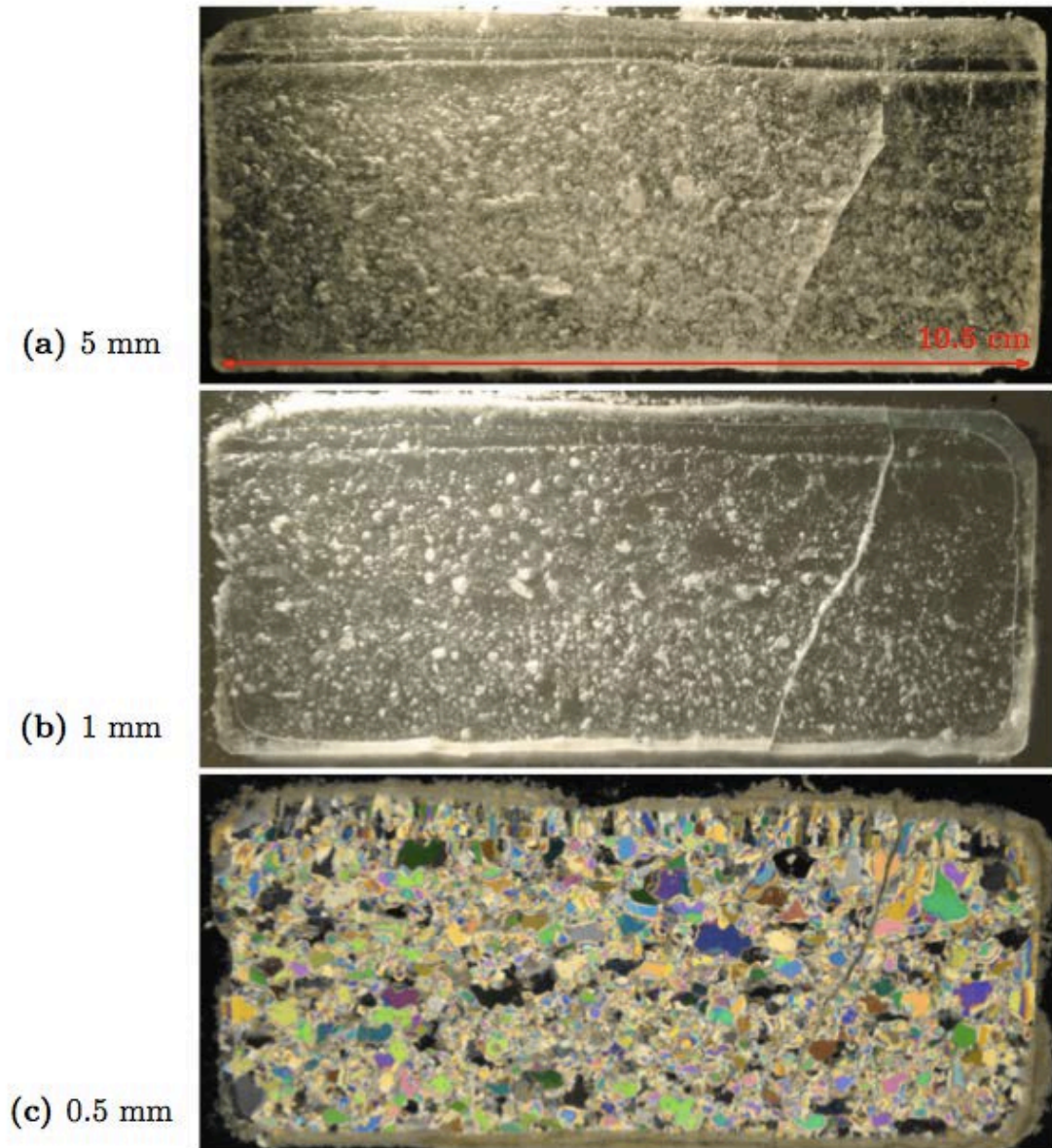


Figure 6: Thick (a, 5mm) and thin (b, 1mm, and c, 0.5mm) sections of undeformed ice, $T_i = -7^\circ\text{C}$. The large crack on the right hand side of the images occurred during sample preparation on the bandsaw. The section shown is 105mm wide.

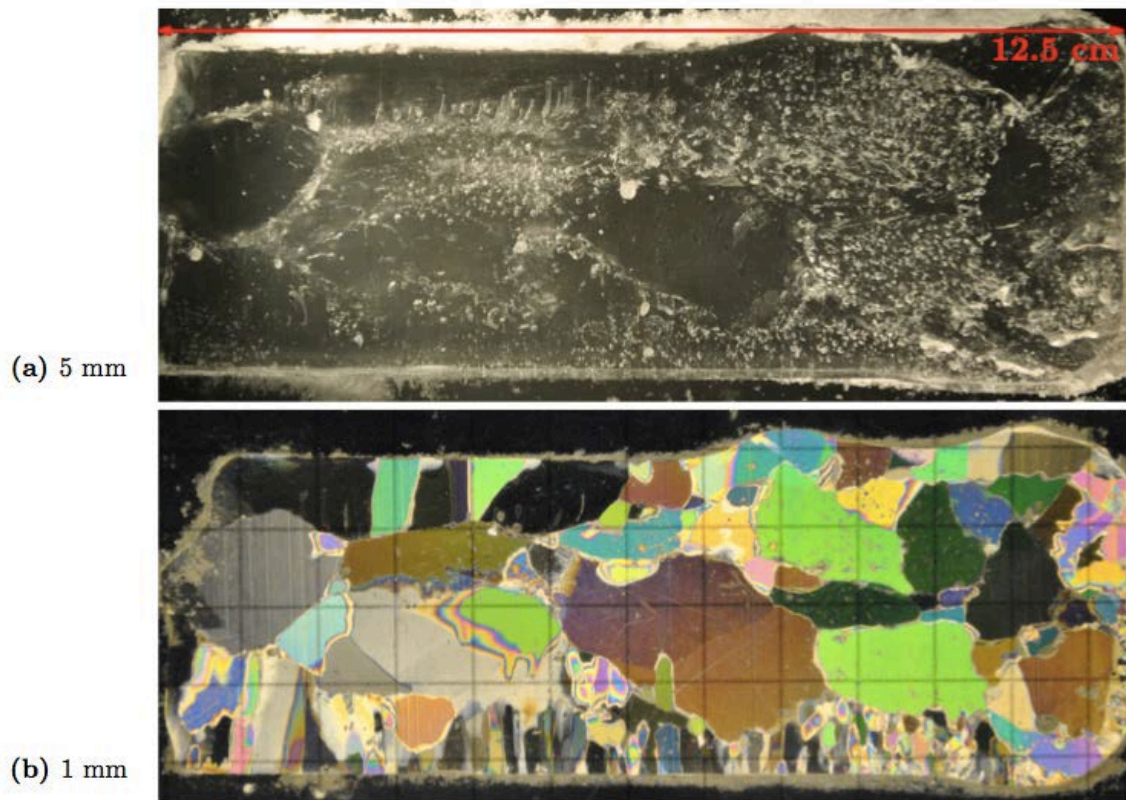


Figure 7: Thick (a, 5mm) and thin (b, 1mm) sections of undeformed ice, $T_i = -0.5^\circ\text{C}$, ice seeds $>3.35\text{mm}$. The section shown is 125mm wide.

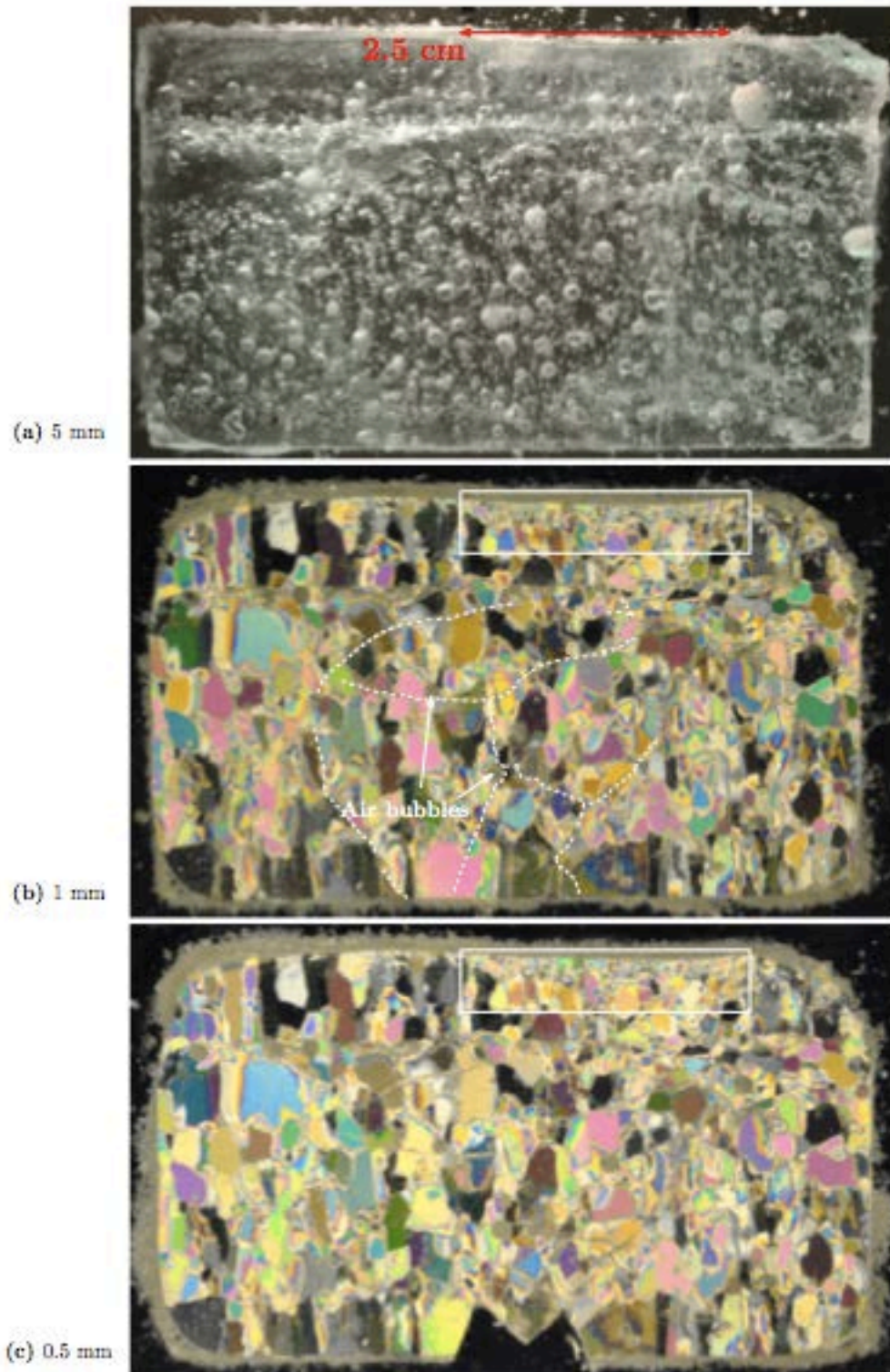
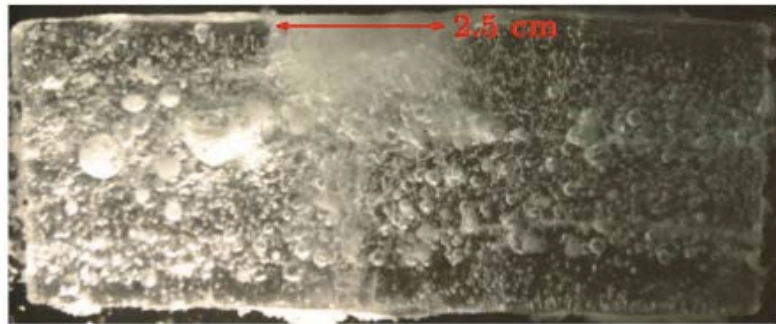
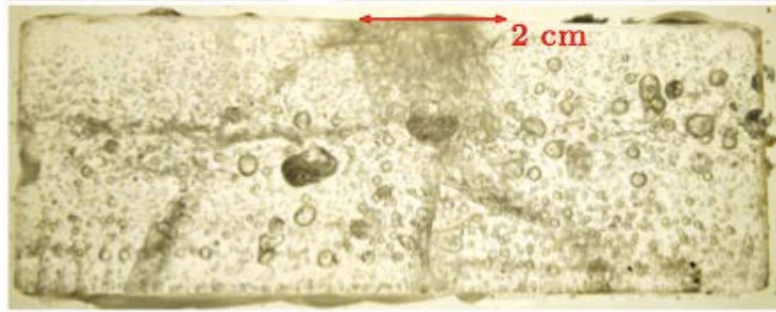


Figure 8: Thick (a, 5mm) and thin (b, 1mm, and c, 0.5mm) sections of deformed ice, $T_i = -0.5^\circ\text{C}$. The extent of deformation is visible in (a) and cracking, which occurred around meltwater during manufacturing, is highlighted in (b). Recrystallisation under the slider is highlighted in the white box.

(a) 5 mm, sample 1



(b) 5 mm, sample 2

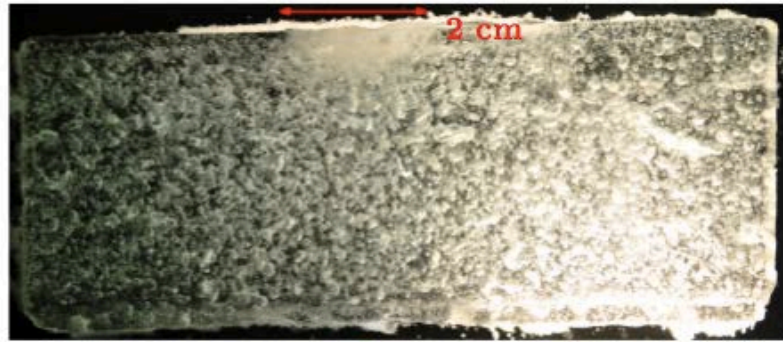


(c) 1 mm, sample 2

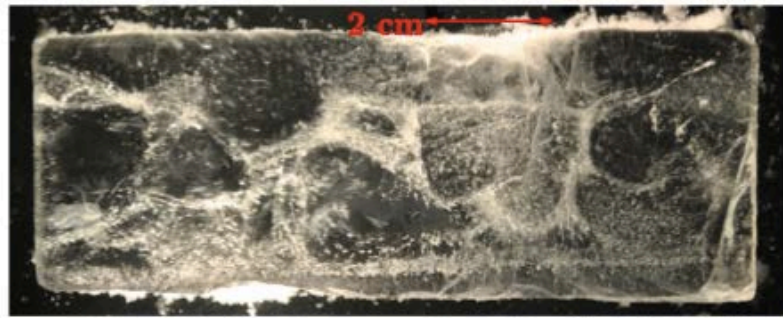


Figure 9: Thick (a, 5mm, sample 1, and b, 5mm, sample 2) and thin (c, 1mm, sample 2) sections of deformed ice, $T_i = -3^\circ\text{C}$, for two different samples (sample 1 is small-grained; sample 2 is large-grained). A damaged zone under the slider is visible in both samples, and fracture networks have propagated through sample 2. Neither recrystallisation nor fracture networks were seen through crossed polars.

(a) 5 mm, sample 1



(b) 5 mm, sample 2



(c) 1 mm, sample 2



Figure 10: Thick (**a**, 5mm, sample 1, and **b**, 5mm, sample 2) and thin (**c**, 1mm, sample 2) sections of deformed ice, $T_i = -7^\circ\text{C}$, for two different samples (sample 1 is small-grained, and sample 2 is large-grained). A damaged zone under the slider is visible in both samples, and fracture networks have propagated through sample 2. Neither recrystallisation nor fracture networks were seen through crossed polars.

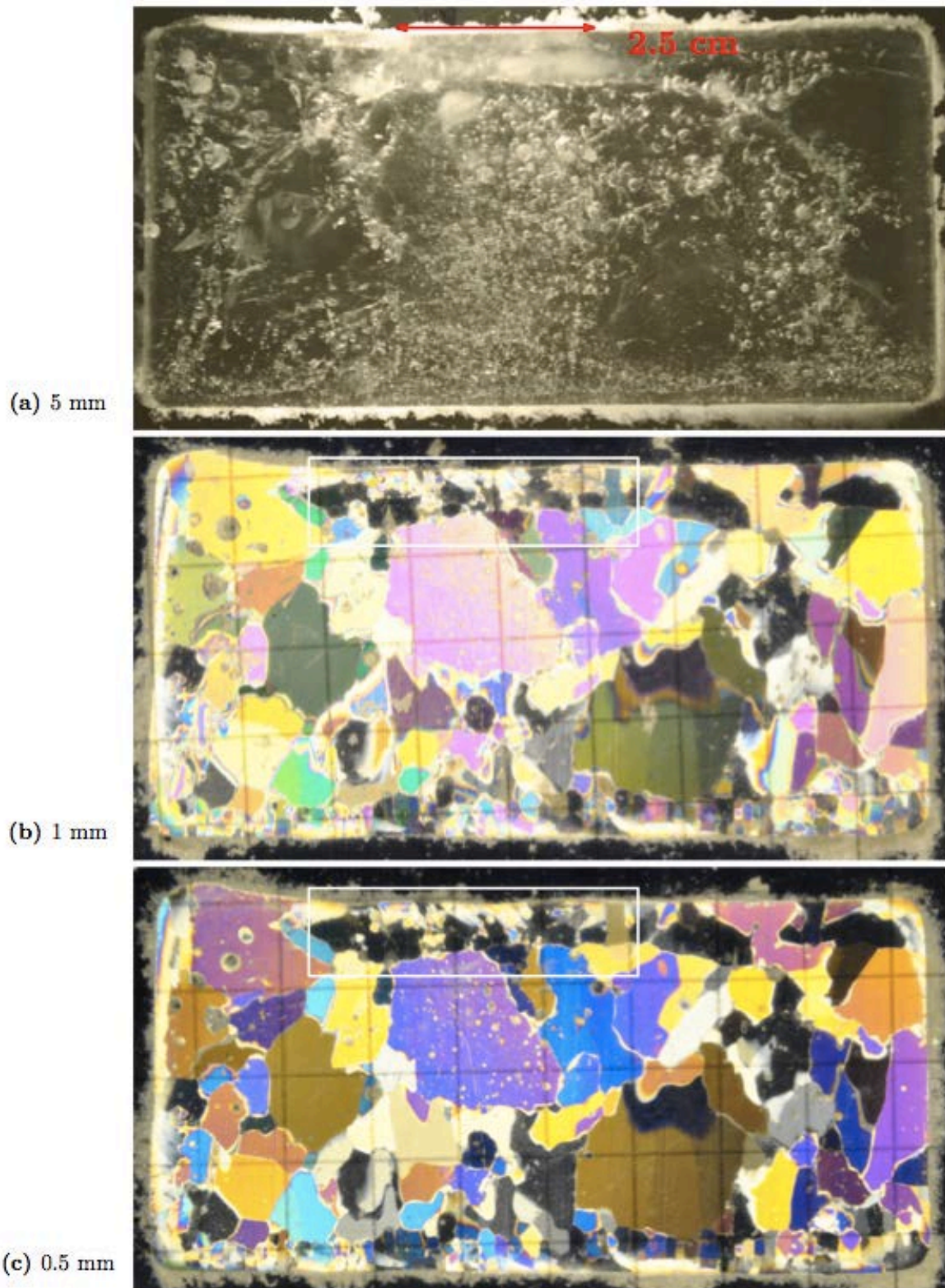
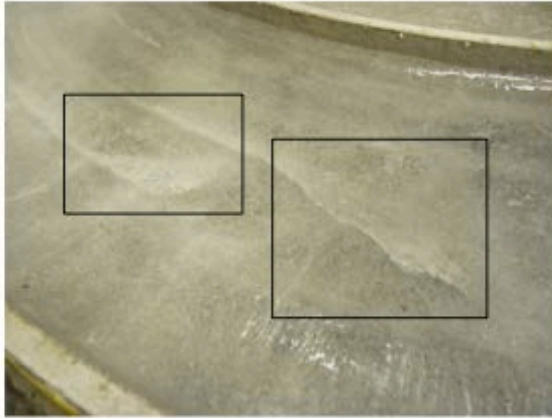
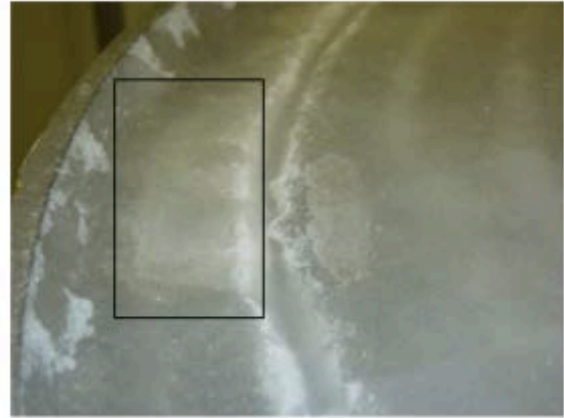


Figure 11: Thick (a, 5mm) and thin (b, 1mm, and c, 0.5mm) sections of deformed ice, $T_i = -0.5^\circ\text{C}$, for seed grain size $>3.35\text{mm}$. Recrystallisation under the slider is highlighted.



(a) $T_i = -0.5^\circ\text{C}$, $v = 6 \text{ m/s}$



(b) $T_i = -3^\circ\text{C}$, $v = 10 \text{ m/s}$



(c) $T_i = -10^\circ\text{C}$, $v = 10 \text{ m/s}$

Figure 12: Illustration of the different types of cracks visible on the ice surface after high speed sliding: (a) $T_i = -0.5^\circ\text{C}$, $v = 6 \text{ m/s}$; (b) $T_i = -3^\circ\text{C}$, $v = 10 \text{ m/s}$; (c) $T_i = -10^\circ\text{C}$, $v = 10 \text{ m/s}$.



(a) Brittle failure



(b) Large cracks



(c) Micro-cracking

Figure 13: Illustration of the inelastic deformation mechanisms observed on the skeleton track: (a) brittle failure, evidenced by sharp-edged cavities in the ice; (b) large cracks, several centimetres long; (c) micro-cracking, evidenced by a milky-white zone, occurring frequently in high- g corners.

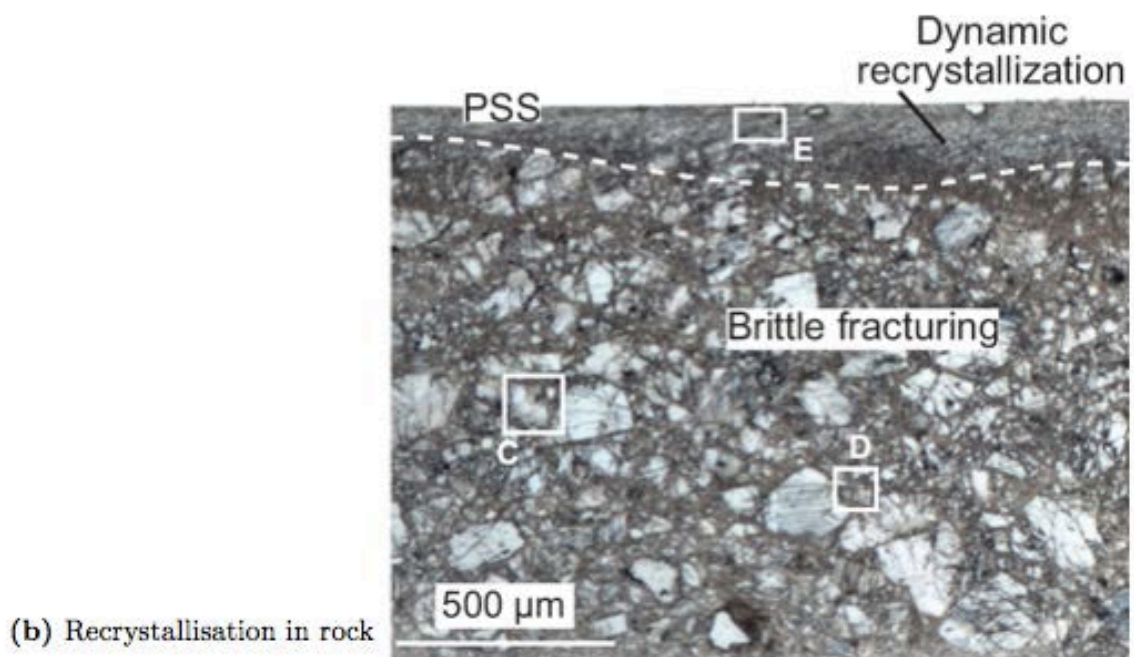
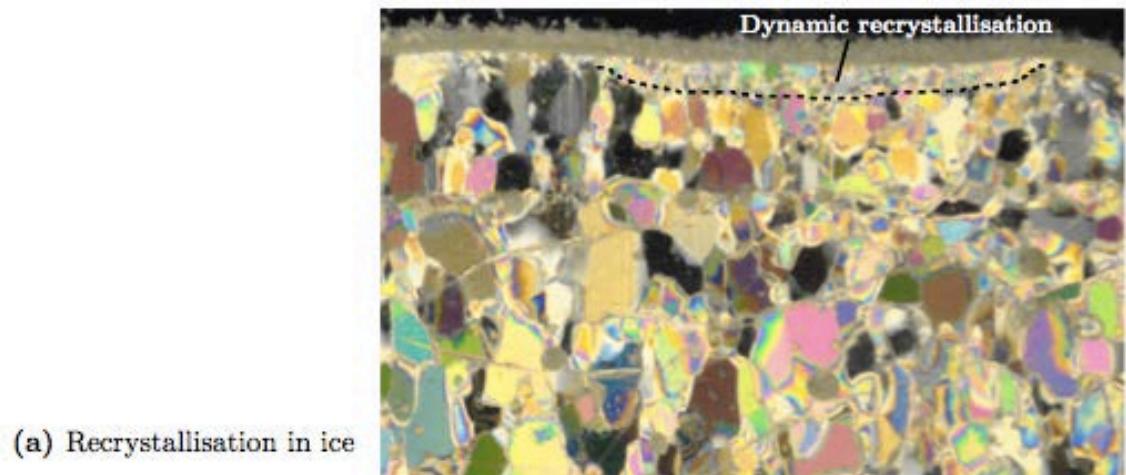


Figure 14: Comparison of recrystallisation mechanisms in ice (a, this study) and rock (b). The ice thin sections are from this study, recrystallisation in rock from Smith et al. (2013).